

Pressure-induced Superconductivity in Zintl Topological Insulator

SrIn_2As_2

Weizheng Cao^{1#}, Haifeng Yang^{1,2#}, Yongkai Li^{3,4,5#}, Cuiying Pei¹, Qi Wang^{1,2}, Yi Zhao¹, Changhua Li¹, Mingxin Zhang¹, Shihao Zhu¹, Juefei Wu¹, Lili Zhang⁶, Zhiwei Wang^{3,4,5*}, Yugui Yao^{3,4}, Zhongkai Liu^{1,2*}, Yulin Chen^{1,2,7}, and Yanpeng Qi^{1,2,8*}

1. School of Physical Science and Technology, ShanghaiTech University, Shanghai 201210, China
2. ShanghaiTech Laboratory for Topological Physics, ShanghaiTech University, Shanghai 201210, China
3. Centre for Quantum Physics, Key Laboratory of Advanced Optoelectronic Quantum Architecture and Measurement (MOE), School of Physics, Beijing Institute of Technology, Beijing 100081, China
4. Beijing Key Lab of Nanophotonics and Ultrafine Optoelectronic Systems, Beijing Institute of Technology, Beijing 100081, China
5. Material Science Center, Yangtze Delta Region Academy of Beijing Institute of Technology, Jiaxing, 314011, China
6. Shanghai Synchrotron Radiation Facility, Shanghai Advanced Research Institute, Chinese Academy of Sciences, Shanghai 201203, China
7. Department of Physics, Clarendon Laboratory, University of Oxford, Parks Road, Oxford OX1 3PU, UK
8. Shanghai Key Laboratory of High-resolution Electron Microscopy, ShanghaiTech University, Shanghai 201210, China

These authors contributed to this work equally.

* Correspondence should be addressed to Y.Q. (qiyp@shanghaitech.edu.cn) Z.L. (liuzhk@shanghaitech.edu.cn) or Z.W. (zhiweiwang@bit.edu.cn)

ABSTRACT

The Zintl compound $A\text{In}_2X_2$ ($A = \text{Ca}, \text{Sr}$, and $X = \text{P}, \text{As}$), as a theoretically predicted new non-magnetic topological insulator, requires experiments to understand their electronic structure and topological characteristics. In this paper, we systematically investigate the crystal structures and electronic properties of the Zintl compound SrIn_2As_2 under both ambient and high-pressure conditions. Based on systematic angle-resolved photoemission spectroscopy (ARPES) measurements, we observed the topological surface states on its (001) surface as predicted by calculations, indicating that SrIn_2As_2 is a strong topological insulator. Interestingly, application of pressure effectively tuned the crystal structure and electronic properties of SrIn_2As_2 . Superconductivity is observed in SrIn_2As_2 for pressure where the temperature dependence of the resistivity changes from a semiconducting-like behavior to that of a metal. The observation of nontrivial topological states and pressure-induced superconductivity in SrIn_2As_2 provides crucial

insights into the relationship between topology and superconductivity, as well as stimulates further studies of superconductivity in topological materials.

INTRODUCTION

Topological insulator (TI) is a novel class of materials that possess both gapped bulk and exotic metallic surface states. The robust topological surface state (TSS) in TI has been confirmed by angle resolved photoemission spectroscopy (ARPES) [1, 2] and scanning tunneling microscopy (STM) [3-5], which also characterized by magneto transport such as Shubnikov – de Hass (SdH) oscillation [6, 7], etc. Due to the dissipationless flow of electric current at the surface, TI has been projected as promising candidates for developing next-generation, low-power-consuming, high-speed electronic, optoelectronic, and spintronic devices. The interplay between symmetry and topology in crystalline solids leads to other emerging topological quantum materials (TQMs), including topological crystalline insulators [8, 9], higher-order topological insulators [10, 11], Dirac [12, 13], Weyl [2, 14-16], nodal line [17, 18], and multifold semimetals [19, 20].

Since first discovery in the early 1900s by Eduard Zintl [21], Zintl compounds have been extensively studied for their fascinating physical properties, including superconductivity, colossal magnetoresistance, magnetic order, mixed-valence, thermoelectricity, and so on [22-28]. Several Zintl compounds have recently garnered attention due to their interesting topological properties. For instance, EuIn_2As_2 exhibits A - type antiferromagnetic (AFM) ordering at $T_N \sim 16$ K [29], and is predicted to be a promising candidate of the axion topological insulator [30]. ARPES results indicated a hole - type Fermi pocket around the Brillouin zone and the AFM transition accompanied by the axion insulator phase [31, 32]. The magnetotransport characterization revealed an anomalous Hall effect (AHE) originated from a nonvanishing Berry curvature and a large topological Hall effect (THE), which is attributed to the scalar spin chirality of the noncoplanar spin structure caused by the external field [33]. Another Zintl compound, SrIn_2As_2 , which is isostructural with EuIn_2As_2 , has been predicted to be a dual topological insulator with nontrivial $Z_2 = 1$ and mirror Chern number $C_M = -1$ via first principles calculations together with symmetry analysis [34]. Furthermore, $A\text{In}_2X_2$ ($A = \text{Ca}, \text{Sr}$, and $X = \text{P}, \text{As}$) family exhibits a narrow band gap which can be easily tuned by high pressure or chemical doping [35-38]. Theoretical calculations indicated that the pressure-induced band gap reduces to zero at 6.6 GPa and then reopens, and SrIn_2As_2 exhibit a gapless non-trivial topological surface state, indicating a strong topological insulator [39]. However, these theoretical predictions have not been experimentally verified yet, and further investigation of the evolution of the physical properties of $A\text{In}_2X_2$ under pressure is required.

In this work, we choose Zintl compound SrIn_2As_2 , one member of the $A\text{In}_2X_2$ family, to systematically investigate the crystal structures and electronic properties under both ambient and high-pressure conditions. The transport measurements reveal metallic behavior for SrIn_2As_2 with hole-dominated carriers. ARPES results demonstrate topological Dirac surface states on the (001) surface, which is consistent with previous theoretical calculation. Interestingly, superconductivity was observed at around 30 GPa and persisted approximately 2.1 K until the maximum experimental pressure. The pressure-induced structure phase transition in the Zintl compound SrIn_2As_2 is also discussed.

EXPERIMENTAL DETAILS

The single crystals of SrIn_2As_2 were grown by self-flux method. High-purity starting materials of Sr, In, and As were loaded in a quartz tube with the ratio of Sr : In : As = 1 : 12 : 2. The tube was sealed after it was evacuated to a vacuum of 2×10^{-4} Pa. The raw materials were reacted and homogenized at 1373 K for several hours, followed by cooling down to 873 K at a rate of 2 K/h. Finally, Shiny crystal with apparent hexagonal edge was obtained after the indium flux was removed by centrifuge. The crystalline phase of SrIn_2As_2 was checked by the single-crystalline x-ray diffraction (XRD, $\text{Cu } K_\alpha$, $\lambda = 1.54184 \text{ \AA}$). The chemical composition value of SrIn_2As_2 is given by energy-dispersive x-ray spectra (EDX). Transmission electron microscopy (TEM) measurements are carried out on a SrIn_2As_2 sample after high-pressure treated at 61.5 GPa. Electrical transport properties including resistivity, magnetoresistance, and Hall effect were performed on a physical property measurement system (PPMS).

In order to investigate the band structures of SrIn_2As_2 , we performed systematic synchrotron-based ARPES measurements at BL03U of Shanghai Synchrotron Radiation Facility. Data were recorded by a Scienta Omicron DA30L analyzer. The measurement sample temperature and pressure were 15 K and 7×10^{-11} mbar, respectively. The overall energy and angle resolutions are ~ 10 meV and 0.2° , respectively. Fresh (001) surfaces were obtained for measurements by *in situ* cleaving the crystals at low temperatures. No signatures of the surface aging were observed during measurements.

High-pressure electrical transport measurements were performed in a nonmagnetic diamond anvil cell (DAC) [40-43]. A cubic BN/epoxy mixture layer was inserted between BeCu gaskets and electrical leads. Four platinum sheet electrodes were touched to the sample for resistance measurements with the van der Pauw method. Pressure was determined by the ruby luminescence method [44]. An *in situ* high-pressure Raman spectroscopy investigation was performed using a Raman spectrometer (Renishaw in-Via, UK) with a laser excitation wavelength of 532 nm and a low-wavenumber filter. A symmetric DAC with anvil culet sizes of 200 μm was used, with silicon oil as pressure transmitting medium (PTM). *In situ* high-pressure XRD measurements were performed at beamline BL15U of Shanghai Synchrotron Radiation Facility (x-ray wavelength $\lambda = 0.6199 \text{ \AA}$). A symmetric DAC with anvil culet sizes of 200 μm and Re gaskets were used. Silicon oil was used as the PTM and pressure was determined by the ruby luminescence method [44]. The two-dimensional diffraction images were analyzed using the FIT2D software [45]. Rietveld refinements of crystal structure under various pressures were performed using the GSAS and the graphical user interface EXPGUI [46, 47].

RESULTS AND DISCUSSION

Figure 1(a) shows the crystal structure of SrIn_2As_2 , which adopts a hexagonal structure with a space group $P6_3/mmc$. The In and As atoms form two layers of a two-dimensional zigzag honeycomb lattice with mirror symmetry, forming $[\text{In}_2\text{As}_2]^{2-}$ polyanions through staggered stacking. Layers of Sr^{2+} and $[\text{In}_2\text{As}_2]^{2-}$ are alternately stacked along the [0 0 1] direction. The single crystal XRD pattern of SrIn_2As_2 displays sharp [0 0 1] diffraction peaks [Figure 1(b)]. The extracted lattice parameter is $c = 18.08 \text{ \AA}$, which is consistent with previous report [35]. Chemical composition analysis from EDX measurement on the single crystal reveals a good stoichiometry with atomic percentage of Sr : In : As = 19.96 : 40.93: 39.10, as shown in the inset of Figure 1(b). These

characterizations indicate a high quality of our samples.

Next, we carried out transport measurements at ambient pressure. Figure 1(c) shows the temperature dependence of resistivity for SrIn₂As₂, which reveals metallic behavior with residual resistivity ratio (RRR) = 2.11. The longitudinal resistivity (ρ_{xx}) and Hall resistivity (ρ_{yx}) were measured with the magnetic field applied along *c*-axis at various temperature ranging from 1.8 K to 300 K, as shown in Figure S1. The positive magnetoresistance is observed in all the temperature range and reaches $\sim 0.47\%$ at 1.8 K and 9 T. At 1.8 K, ρ_{yx} displays a linear dependence on the magnetic field with a positive slope, indicating that the hole carriers play a dominant role in the transport. This is also consistent with our ARPES measurements shown below. However, ρ_{yx} shows almost temperature independent with a rather slight change over the measured temperature range. Hall resistivity is fitted using single-band model, i.e., $\rho_{yx} = R_H B$, where $R_H = 1/en$ is the Hall coefficient. Figure 1(d) shows the temperature dependence of carrier density *n* and carrier mobility μ . The carrier density *n* reaches $3.58 \times 10^{25} \text{ m}^{-3}$ and carrier mobility μ is estimated to be $343.94 \text{ cm}^2 \cdot \text{V}^{-1} \cdot \text{s}^{-1}$ at 1.8 K, which are comparable with other topological materials [48].

Figure 2(a) and (b) display the measured constant-energy contours of SrIn₂As₂. The Fermi surface of SrIn₂As₂ is mainly composed of a circle encircling the $\bar{\Gamma}$ point. Inside the circle, some blurry features are also discernable. When going towards high-binding-energy regions, the circle keeps expanding, and circles from other adjacent Brillouin zones connect with each other to form a hexagon, consistent with the crystal symmetry of (001) surface. If cutting the Fermi surface along $\bar{\Gamma}$ - \bar{M} direction, one can see the sharp hole-like band dispersion marked as α that contributes to the circle Fermi surface, and multiple blurry bands residing between the two α bands [Figures 2(c) and (d)]. These dispersions exhibit qualitative agreement with previous theoretical calculations proposing SrIn₂As₂ is a dual topological insulator and hosts topological Dirac surface states on the (001) surface [Figure 2 (e)] [34]. However, we have not observed the whole Dirac surface states dispersion (including the Dirac point) as the crystals appear to be heavily *p*-doped compared to the calculations (the red dotted line is the Fermi level from experiments in Figure 2(e)). We tried *in-situ* potassium dosing but the shift-up of the Fermi level is quite limited. We ascribe the observed α bands to be the tail of the Dirac surface states. Their surface state nature is further verified by the detailed photon-energy dependence measurements as they show negligible k_z -dispersions [Figure 2(f)].

The Zintl compound SrIn₂As₂ with narrow band gap is extremely sensitive to external pressure. In addition, first principles calculations indicate that SrIn₂As₂ will undergo insulator–metal phase transition and topological quantum phase transition under pressure modulation. Indeed, the high-pressure approach has been widely employed in recent studies of topological materials and has led to many interesting results [49-51]. Hence, we are motivated to investigate the effect of high pressure on the electrical transport properties of SrIn₂As₂. Figure 3 shows temperature dependence of the electrical resistivity $\rho(T)$ of SrIn₂As₂ for pressure up to 70.9 GPa. At low pressure region, the $\rho(T)$ first decrease with decrease temperature and reaches a minimum value. Then the $\rho(T)$ gradually increases showing semiconducting-like behavior at 2.8 GPa with a negative $d\rho/dT$ slope [Figure 3(a)]. The anomalous $\rho(T)$ of SrIn₂As₂ implies that the carriers are weak localized at low temperature due to strong quantum coherence [38]. Upon further increasing the pressure, the resistivity at 300 K begins to decrease rapidly and the semiconducting-like behavior is suppressed accompanied by a drop of $\rho(T)$ at the lowest temperature ($T_{\min} = 1.8 \text{ K}$), as show in the inset of Figure 3(a). With

pressure increasing, the drop of $\rho(T)$ becomes more pronounced and zero resistivity is achieved at low temperature for $P > 53.9$ GPa, indicating the emergence of superconducting transition. Moreover, the superconductivity with $T_c \sim 2.1$ K is robust and persists until the maximum pressure of 70.9 GPa [Figure 3(b)].

To gain insights into the superconducting transition, we applied external magnetic field on SrIn₂As₂ at 48.9 GPa and 59.8 GPa, respectively. It is clear that magnetic field could suppress superconducting transition (Inset of Figure 3(d)). T_c gradually shifts toward lower temperature with the increase of the magnetic field. A magnetic field $\mu_0 H = 0.5$ T removes all signs of superconductivity above 1.8 K as shown in Figure 3(c). These results further confirm pressure-induced bulk superconductivity in SrIn₂As₂. The derived upper critical field $\mu_0 H_{c2}$ as a function of temperature can be well fitted using the empirical Ginzburg-Landau formula $\mu_0 H_{c2}(T) = \mu_0 H_{c2}(0) (1 - t^2)/(1 + t^2)$, where $t = T/T_c$ is the reduced temperature with zero-field superconducting T_c . The extrapolated upper critical field $\mu_0 H_{c2}(0)$ of SrIn₂As₂ from 90% ρ_n criterion can reach 1.35 T at 59.8 GPa, which yields a Ginzburg-Landau coherence length $\xi_{GL}(0)$ of 15.60 nm. It is worth noting that the value of $\mu_0 H_{c2}(0)$ is well below the Pauli-Clogston limit.

To further identify the origin of superconductivity in SrIn₂As₂, *in situ* x-ray diffraction (XRD) measurements have been carried out to analysis the structure evolution under various pressures. Figure 4(a) shows the high-pressure synchrotron XRD patterns measured at room temperature up to 71.7 GPa. A representative refinement at 3.9 GPa is displayed in Figure S3(a). At lower pressure region, all the diffraction peaks can be indexed well to the hexagonal structure with a space group $P6_3/mmc$. The small peaks marked with an asterisk represent the signal of the rhenium gasket, which is caused by the dragging of the x-ray spot. Further increase of the applied pressure gives rise to the shift of the Bragg peaks to larger angles, due to the lattice shrinkage, as shown in the pressure dependences of the lattice parameters in Figure S3(b). The experience pressure-volume ($P - V$) data can be well fitted using the third-order Birch-Murnaghan equation of state (EOS) [52], which obtained bulk modulus K_0 is 58.32 GPa with $V_0 = 277.91 \text{ \AA}^3$ and $K'_0 = 5.80$. The structure of SrIn₂As₂ is robust and there is no structural phase transition until 23.2 GPa. However, when the pressure increases up to 30.8 GPa, a broad peak appears around 14.4° in the diffraction patterns, indicating the application of high-pressure introduced amorphous phases in the SrIn₂As₂. A similar phenomenon was observed in some other materials [49, 51, 53-58]. It should be mentioned that the superconductivity is observed where pressure increase up to 30 GPa. To derive more structural information, high pressure *in situ* Raman spectroscopy measurements were carried out. As shown in Figure 4(c), Raman active modes are clearly observed at lower pressure regions. With increasing pressure, the profile of the spectra remains similar to that at lower pressure, whereas the observed modes exhibit blue shift, thus showing the normal pressure behavior. An abrupt disappearance of Raman peaks for pressure near to 23.7 GPa indicates the structural phase transition to an amorphous phase. The evolution of the Raman spectra is consistent with our synchrotron XRD patterns.

Several independent high-pressure transport measurements on SrIn₂As₂ single crystals provide consistent and reproducible results, confirming intrinsic superconductivity under high-pressure. From resistivity, XRD and Raman measurements, we can construct a T - P phase diagram of SrIn₂As₂ (Figure 5). In the lower pressure region, the $\rho(T)$ decreases upon cooling in a metallic manner firstly and then undergoes a minimum value. Subsequently, the $\rho(T)$ upturns rapidly just like a semiconductor characteristic. Such anomalous $\rho(T)$ behavior due to weak localization effect

provides a signal of quantum correction to conductance in SrIn₂As₂ [38]. Upon further increasing the pressure, the resistivity at room temperature as well as 3 K begins to drop rapidly and the semiconductor-like behavior is suppressed. Superconductivity is observed after the temperature dependence of $\rho(T)$ changes from a semiconducting-like behavior to that of a metal. The T_c of SrIn₂As₂ rises to 2.1 K and persists until the maximum pressure of this work. Above 30 GPa, *in situ* high pressure XRD demonstrated that a pressure-induced amorphization emerges. High pressure amorphous phase of SrIn₂As₂ retain after the pressure released, which confirmed by TEM measurements (Figures S3(c) and (d)). It is very interesting that an amorphous phase of SrIn₂As₂ could support superconductivity. This will be a stimulus for further research from an experimental and theoretical point of view.

CONCLUSION

In summary, we have successfully grown high-quality single crystal of the Zintl compound SrIn₂As₂. Combining the transports and ARPES measurements, we indicate that SrIn₂As₂ is a strong topological insulator. Moreover, we discovered pressure-induced superconductivity in SrIn₂As₂, and T_c still persists until a maximum experimentally pressure. Our results demonstrate that the nontrivial topological state and the pressure-induced superconductivity were all observed in SrIn₂As₂. Thus, the Zintl $A\text{In}_2X_2$ ($A = \text{Ca}, \text{Sr}$, and $X = \text{P}, \text{As}$) family provides an excellent platform for further understanding the relationship between the topological phase and superconductivity.

ACKNOWLEDGMENT

This work was supported by the National Natural Science Foundation of China (Grant Nos. 52272265, U1932217, 11974246, 12004252), the National Key R&D Program of China (Grant No. 2018YFA0704300), and Shanghai Science and Technology Plan (Grant No. 21DZ2260400). H.F.Y. thanks the support from Shanghai Sailing Program (20YF1430500), the National Natural Science Foundation of China (Grant No. 12004248). Z.K.L. acknowledges the Technology Innovation Action Plan of the Science and Technology Commission of Shanghai Municipality with project number 20JC1416000. Z.W.W. thanks the support from the National Key R&D Program of China (Grant Nos. 2020YFA0308800 and 2022YFA1403400), the Natural Science Foundation of China (Grant No. 92065109), the Beijing Natural Science Foundation (Grant Nos. Z210006 and Z190006). The authors thank the Analytical Instrumentation Center (# SPST-AIC10112914), SPST, ShanghaiTech University and the Analysis and Testing Center at Beijing Institute of Technology for assistance in facility support. The authors thank the staffs from BL15U1 at Shanghai Synchrotron Radiation Facility for assistance during data collection.

REFERENCES

- [1] B. Lv, N. Xu, H. Weng, J. Ma, P. Richard, X. Huang, L. Zhao, G. Chen, C. Matt, F. Bisti, Observation of Weyl nodes in TaAs, *Nature Physics*, 11 (2015) 724-727.
- [2] S.Y. Xu, I. Belopolski, N. Alidoust, M. Neupane, G. Bian, C. Zhang, R. Sankar, G. Chang, Z. Yuan, C.-C. Lee, Discovery of a Weyl fermion semimetal and topological Fermi arcs, *Science*, 349 (2015) 613-617.
- [3] C.L. Song, Y.P. Jiang, Y.L. Wang, Z. Li, L. Wang, K. He, X. Chen, X.C. Ma, Q.K. Xue, Gating the charge state of single Fe dopants in the topological insulator Bi₂Se₃ with a scanning tunneling

- microscope, *Phys. Rev. B*, 86 (2012) 045441.
- [4] M. Chen, J.-P. Peng, H.M. Zhang, L.L. Wang, K. He, X.C. Ma, Q.K. Xue, Molecular beam epitaxy of bilayer Bi (111) films on topological insulator Bi_2Te_3 : A scanning tunneling microscopy study, *Appl. Phys. Lett.*, 101 (2012) 081603.
- [5] X.B. Li, W.K. Huang, Y.-Y. Lv, K.W. Zhang, C.L. Yang, B.B. Zhang, Y. Chen, S.H. Yao, J. Zhou, M.H. Lu, Experimental observation of topological edge states at the surface step edge of the topological insulator ZrTe_5 , *Phys. Rev. Lett.*, 116 (2016) 176803.
- [6] G. Eguchi, K. Kuroda, K. Shirai, A. Kimura, M. Shiraishi, Surface Shubnikov–de Haas oscillations and nonzero Berry phases of the topological hole conduction in $\text{Tl}_{1-x}\text{Bi}_{1+x}\text{Se}_2$, *Phys. Rev. B*, 90 (2014) 201307.
- [7] L. Fang, Y. Jia, D. Miller, M. Latimer, Z. Xiao, U. Welp, G. Crabtree, W.K. Kwok, Catalyst-free growth of millimeter-long topological insulator Bi_2Se_3 nanoribbons and the observation of the π -Berry phase, *Nano letters*, 12 (2012) 6164–6169.
- [8] L. Fu, Topological crystalline insulators, *Phys. Rev. Lett.*, 106 (2011) 106802.
- [9] T.H. Hsieh, H. Lin, J. Liu, W. Duan, A. Bansil, L. Fu, Topological crystalline insulators in the SnTe material class, *Nat. Commun.*, 3 (2012) 982.
- [10] F. Schindler, A.M. Cook, M.G. Vergniory, Z. Wang, S.S. Parkin, B.A. Bernevig, T. Neupert, Higher-order topological insulators, *Sci. Adv.*, 4 (2018) eaat0346.
- [11] F. Schindler, Z. Wang, M.G. Vergniory, A.M. Cook, A. Murani, S. Sengupta, A.Y. Kasumov, R. Deblock, S. Jeon, I. Drozdov, Higher-order topology in bismuth, *Nature physics*, 14 (2018) 918–924.
- [12] Z. Liu, B. Zhou, Y. Zhang, Z. Wang, H. Weng, D. Prabhakaran, S.K. Mo, Z. Shen, Z. Fang, X. Dai, Discovery of a three-dimensional topological Dirac semimetal, Na_3Bi , *Science*, 343 (2014) 864–867.
- [13] Z. Liu, J. Jiang, B. Zhou, Z. Wang, Y. Zhang, H. Weng, D. Prabhakaran, S.K. Mo, H. Peng, P. Dudin, A stable three-dimensional topological Dirac semimetal Cd_3As_2 , *Nat. Mater.*, 13 (2014) 677–681.
- [14] B. Lv, H. Weng, B. Fu, X.P. Wang, H. Miao, J. Ma, P. Richard, X. Huang, L. Zhao, G. Chen, Experimental discovery of Weyl semimetal TaAs, *Phys. Rev. X*, 5 (2015) 031013.
- [15] S.Y. Xu, N. Alidoust, G. Chang, H. Lu, B. Singh, I. Belopolski, D.S. Sanchez, X. Zhang, G. Bian, H. Zheng, Discovery of Lorentz-violating type II Weyl fermions in LaAlGe , *Sci. Adv.*, 3 (2017) e1603266.
- [16] W. Cao, Y. Su, Q. Wang, C. Pei, L. Gao, Y. Zhao, C. Li, N. Yu, J. Wang, Z. Liu, Quantum oscillations in noncentrosymmetric Weyl semimetal SmAlSi , *Chin. Phys. Lett.*, 39 (2022) 047501.
- [17] C. Fang, H. Weng, X. Dai, Z. Fang, Topological nodal line semimetals, *Chin. Phys. B*, 25 (2016) 117106.
- [18] C. Fang, Y. Chen, H.Y. Kee, L. Fu, Topological nodal line semimetals with and without spin-orbital coupling, *Phys. Rev. B*, 92 (2015) 081201.
- [19] C. Le, Y. Sun, Topology and symmetry of circular photogalvanic effect in the chiral multifold semimetals: a review, *J. Phys.: Condens. Matter*, 33 (2021) 503003.
- [20] Z. Ni, K. Wang, Y. Zhang, O. Pozo, B. Xu, X. Han, K. Manna, J. Paglione, C. Felser, A.G. Grushin, Giant topological longitudinal circular photo-galvanic effect in the chiral multifold semimetal CoSi , *Nat. Commun.*, 12 (2021) 154.
- [21] E. Zintl, Intermetallische verbindungen, *Angewandte Chemie*, 52 (1939) 1–6.
- [22] N. Varnava, T. Berry, T.M. McQueen, D. Vanderbilt, Engineering magnetic topological

- insulators in $\text{Eu}_5\text{M}_2\text{X}_6$ Zintl compounds, *Phys. Rev. B*, 105 (2022) 235128.
- [23] J. Wang, X. Cui, Y. Wan, T. Ying, S. Li, J. Guo, Superconductivity in layered Zintl phase LiSn_2As_2 , arXiv preprint arXiv:2111.11319, DOI (2021).
- [24] J. Wang, T. Ying, J. Deng, C. Pei, T. Yu, X. Chen, Y. Wan, M. Yang, W. Dai, D. Yang, Superconductivity in an Orbital-Reoriented SnAs Square Lattice: A Case Study of $\text{Li}_{0.6}\text{Sn}_2\text{As}_2$ and NaSnAs , *Angewandte Chemie*, 135 (2023) e202216086.
- [25] T. Qin, R. Zhong, W. Cao, S. Shen, C. Wen, Y. Qi, S. Yan, Real-Space Observation of Unidirectional Charge Density Wave and Complex Structural Modulation in the Pnictide Superconductor $\text{Ba}_{1-x}\text{Sr}_x\text{Ni}_2\text{As}_2$, *Nano Letters*, 23 (2023) 2958-2963.
- [26] Y. Qi, Z. Gao, L. Wang, D. Wang, X. Zhang, Y. Ma, Superconductivity at 34.7 K in the iron arsenide $\text{Eu}_{0.7}\text{Na}_{0.3}\text{Fe}_2\text{As}_2$, *New J. Phys.*, 10 (2008) 123003.
- [27] Z. Gao, Y. Qi, L. Wang, D. Wang, X. Zhang, C. Yao, C. Wang, Y. Ma, Synthesis and properties of La-doped CaFe_2As_2 single crystals with $T_c = 42.7$ K, *Europhysics Letters*, 95 (2011) 67002.
- [28] Y. Qi, Z. Gao, L. Wang, D. Wang, X. Zhang, C. Yao, C. Wang, C. Wang, Y. Ma, Transport properties and anisotropy in rare-earth doped CaFe_2As_2 single crystals with T_c above 40 K, *Superconductor Science and Technology*, 25 (2012) 045007.
- [29] A.M. Goforth, P. Klavins, J.C. Fettinger, S.M. Kauzlarich, Magnetic properties and negative colossal magnetoresistance of the rare earth zintl phase EuIn_2As_2 , *Inorg. Chem.*, 47 (2008) 11048-11056.
- [30] Y. Xu, Z. Song, Z. Wang, H. Weng, X. Dai, Higher-order topology of the axion insulator EuIn_2As_2 , *Phys. Rev. Lett.*, 122 (2019) 256402.
- [31] S. Regmi, M.M. Hosen, B. Ghosh, B. Singh, G. Dhakal, C. Sims, B. Wang, F. Kabir, K. Dimitri, Y. Liu, Temperature-dependent electronic structure in a higher-order topological insulator candidate EuIn_2As_2 , *Phys. Rev. B*, 102 (2020) 165153.
- [32] Y. Zhang, K. Deng, X. Zhang, M. Wang, Y. Wang, C. Liu, J.W. Mei, S. Kumar, E.F. Schwier, K. Shimada, In-plane antiferromagnetic moments and magnetic polaron in the axion topological insulator candidate EuIn_2As_2 , *Phys. Rev. B*, 101 (2020) 205126.
- [33] J. Yan, Z.Z. Jiang, R.C. Xiao, W. Lu, W. Song, X. Zhu, X. Luo, Y. Sun, M. Yamashita, Field-induced topological Hall effect in antiferromagnetic axion insulator candidate EuIn_2As_2 , *Physical Review Research*, 4 (2022) 013163.
- [34] A.B. Sarkar, S. Mardanya, S.-M. Huang, B. Ghosh, C.Y. Huang, H. Lin, A. Bansil, T.R. Chang, A. Agarwal, B. Singh, Magnetically tunable Dirac and Weyl fermions in the Zintl materials family, *Phys. Rev. Mater.*, 6 (2022) 044204.
- [35] M.O. Ogunbunmi, S. Baranets, A.B. Childs, S. Bobev, The Zintl phases AlIn_2As_2 (A= Ca, Sr, Ba): new topological insulators and thermoelectric material candidates, *Dalton Transactions*, 50 (2021) 9173-9184.
- [36] N. Guechi, A. Bouhemadou, A. Guechi, M. Reffas, L. Louail, A. Bourzami, M. Chegaar, S. Bin Omran, First-principles prediction of the structural, elastic, electronic and optical properties of the Zintl phases MIn_2P_2 (M= Ca, Sr), *Journal of alloys and compounds*, 577 (2013) 587-599.
- [37] Z. Wang, G. Wang, X. Shi, D. Wang, X. Tian, Topological phase transition in layered XIn_2P_2 (X= Ca, Sr), *J. Phys. D: Appl. Phys.*, 50 (2017) 465304.
- [38] H. Wang, X. Zhu, Z. Chen, F. Lu, H. Li, Y. Han, L. Li, W. Gao, W. Ning, M. Tian, Weak localization and electron-phonon interaction in layered Zintl phase SrIn_2P_2 single crystal, *J. Phys.: Condens. Matter*, 33 (2021) 245701.

- [39] W.-T. Guo, Z. Huang, J.M. Zhang, The Zintl phase compounds $A\text{In}_2\text{As}_2$ ($A = \text{Ca}, \text{Sr}, \text{Ba}$): topological phase transition under pressure, *Physical Chemistry Chemical Physics*, 24 (2022) 17337-17347.
- [40] C. Pei, T. Ying, Y. Zhao, L. Gao, W. Cao, C. Li, H. Hosono, Y. Qi, Pressure-induced reemergence of superconductivity in BaIr_2Ge_7 and $\text{Ba}_3\text{Ir}_4\text{Ge}_{16}$ with cage structures, *Matter and Radiation at Extremes*, 7 (2022).
- [41] C. Pei, J. Zhang, Q. Wang, Y. Zhao, L. Gao, C. Gong, S. Tian, R. Luo, M. Li, W. Yang, Pressure-induced superconductivity at 32 K in MoB_2 , *National Science Review*, 10 (2023) nwad034.
- [42] C. Pei, T. Ying, Q. Zhang, X. Wu, T. Yu, Y. Zhao, L. Gao, C. Li, W. Cao, Q. Zhang, Caging-pnictogen-induced superconductivity in skutterudites IrX_3 ($X = \text{As}, \text{P}$), *Journal of the American Chemical Society*, 144 (2022) 6208-6214.
- [43] C. Pei, S. Jin, P. Huang, A. Vymazalova, L. Gao, Y. Zhao, W. Cao, C. Li, P. Nemes Incze, Y. Chen, Pressure-induced superconductivity and structure phase transition in Pt_2HgSe_3 , *npj Quantum Mater.*, 6 (2021) 98.
- [44] H. Mao, J.A. Xu, P. Bell, Calibration of the ruby pressure gauge to 800 kbar under quasi-hydrostatic conditions, *J. Geophys. Res. Solid Earth*, 91 (1986) 4673-4676.
- [45] A. Hammersley, S. Svensson, M. Hanfland, A. Fitch, D. Hausermann, Two-dimensional detector software: from real detector to idealised image or two-theta scan, *International Journal of High Pressure Research*, 14 (1996) 235-248.
- [46] A.C. Larson, R.B. Von Dreele, General structure analysis system (GSAS)(Report LAUR 86-748), Los Alamos, New Mexico: Los Alamos National Laboratory, DOI (2004).
- [47] B.H. Toby, EXPGUI, a graphical user interface for GSAS, *J Appl Crystallogr*, 34 (2001) 210-213.
- [48] E. Emmanouilidou, B. Shen, X. Deng, T.R. Chang, A. Shi, G. Kotliar, S.Y. Xu, N. Ni, Magnetotransport properties of the single-crystalline nodal-line semimetal candidates CaTX ($T = \text{Ag}, \text{Cd}$; $X = \text{As}, \text{Ge}$), *Phys. Rev. B*, 95 (2017) 245113.
- [49] Y. Qi, W. Shi, P. Werner, P.G. Naumov, W. Schnelle, L. Wang, K.G. Rana, S. Parkin, S.A. Medvedev, B. Yan, Pressure-induced superconductivity and topological quantum phase transitions in a quasi-one-dimensional topological insulator: Bi_4I_4 , *npj Quantum Mater.*, 3 (2018) 4.
- [50] C. Pei, Y. Xia, J. Wu, Y. Zhao, L. Gao, T. Ying, B. Gao, N. Li, W. Yang, D. Zhang, Pressure-induced topological and structural phase transitions in an antiferromagnetic topological insulator, *Chin. Phys. Lett.*, 37 (2020) 066401.
- [51] W. Cao, N. Zhao, C. Pei, Q. Wang, Q. Zhang, T. Ying, Y. Zhao, L. Gao, C. Li, N. Yu, Pressure-induced superconductivity in the noncentrosymmetric Weyl semimetals LaAlX ($X = \text{Si}, \text{Ge}$), *Phys. Rev. B*, 105 (2022) 174502.
- [52] H. Cynn, J.E. Klepeis, C.S. Yoo, D.A. Young, Osmium has the lowest experimentally determined compressibility, *Phys. Rev. Lett.*, 88 (2002) 135701.
- [53] Y. Zhao, J. Hou, Y. Fu, C. Pei, J. Sun, Q. Wang, L. Gao, W. Cao, C. Li, S. Zhu, Pressure-induced superconductivity in PdTe with quasi-one-dimensional PdTe chains, *Crystals*, 12 (2022) 1833.
- [54] K. Zhang, M. Xu, N. Li, M. Xu, Q. Zhang, E. Greenberg, V.B. Prakapenka, Y.-S. Chen, M. Wuttig, H.-K. Mao, Superconducting phase induced by a local structure transition in amorphous Sb_2Se_3 under high pressure, *Phys. Rev. Lett.*, 127 (2021) 127002.
- [55] Q. Wang, X.-L. Qiu, C. Pei, B.-C. Gong, L. Gao, Y. Zhao, W. Cao, C. Li, S. Zhu, M. Zhang, Superconductivity emerging from a pressurized van der Waals kagome material $\text{Pd}_3\text{P}_2\text{S}_8$, *New J. Phys.*, 25 (2023) 043001.

- [56] W. Li, J. Feng, X. Zhang, C. Li, H. Dong, W. Deng, J. Liu, H. Tian, J. Chen, S. Jiang, Metallization and Superconductivity in the van der Waals Compound CuP_2Se through Pressure-Tuning of the Interlayer Coupling, *Journal of the American Chemical Society*, 143 (2021) 20343-20355.
- [57] Q.-G. Mu, D. Nenno, Y.-P. Qi, F.-R. Fan, C. Pei, M. ElGhazali, J. Gooth, C. Felser, P. Narang, S. Medvedev, Suppression of axionic charge density wave and onset of superconductivity in the chiral Weyl semimetal Ta_2Se_5 , *Phys. Rev. Mater.*, 5 (2021) 084201.
- [58] C. Pei, W. Shi, Y. Zhao, L. Gao, J. Gao, Y. Li, H. Zhu, Q. Zhang, N. Yu, C. Li, Pressure-induced a partial disorder and superconductivity in quasi-one-dimensional Weyl semimetal $(\text{NbSe}_4)_2\text{I}$, *Mater. Today Phys.*, 21 (2021) 100509.

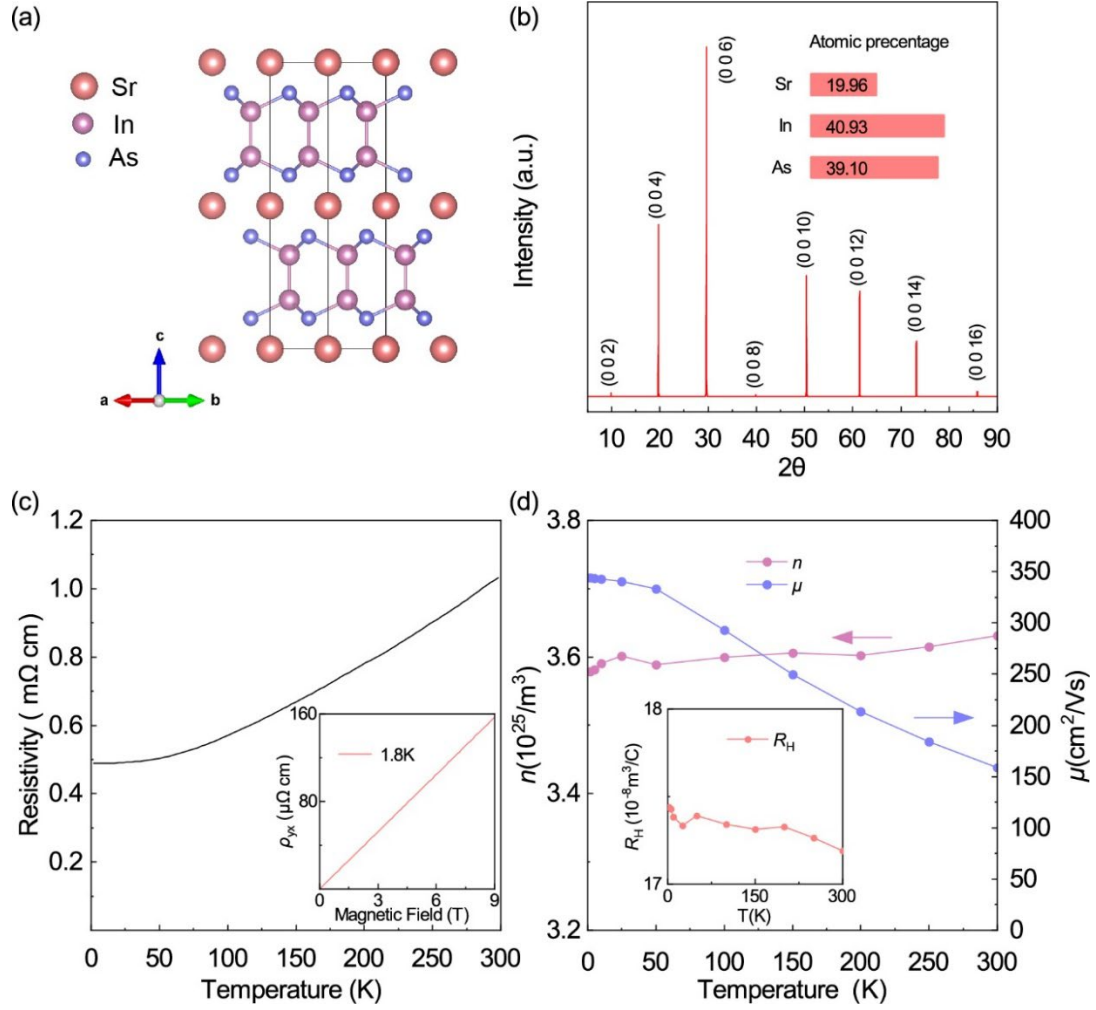


FIG. 1. (a) The crystal structure of SrIn_2As_2 with a space group $P6_3/mmc$. (b) The room-temperature x-ray diffraction peaks from the ab plane of SrIn_2As_2 single crystal. Inset: the elemental content of SrIn_2As_2 . (c) Resistivity of the SrIn_2As_2 single crystal from 1.8 K to 300 K. Inset: Hall resistivity $[\rho_{yx}(H)]$ as a function of magnetic field at 1.8 K with magnetic field applied along the c -axis direction; (d) Carrier density n and mobility μ of SrIn_2As_2 as a function of temperature, respectively. Inset: temperature dependence of Hall coefficient R_H for SrIn_2As_2 .

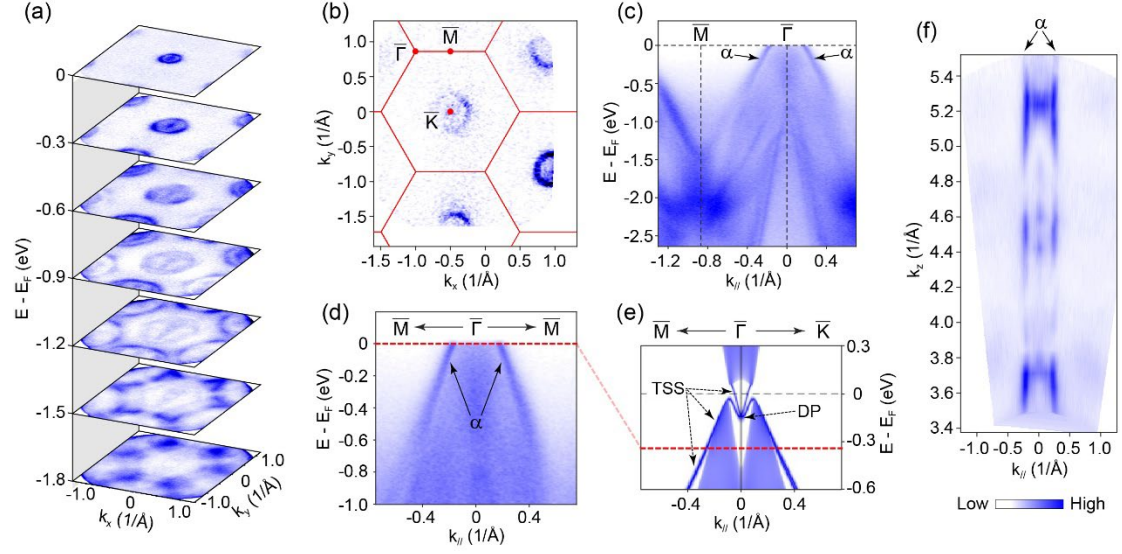


FIG. 2. ARPES measurements on SrIn₂As₂ crystals. (a) Stacking plot of constant energy contours measured in 98 eV photons with linearly horizontal polarization. (b) Fermi surface map across multiple Brillouin zones measured using 110 eV photons. The red lines represent the projected Brillouin zone. (c) High-symmetry band dispersion along the $\bar{\Gamma}$ - \bar{M} direction. (d) Zoom-in of the $\bar{\Gamma}$ - \bar{M} dispersion near the Fermi level. (e) Calculated $\bar{\Gamma}$ - \bar{M} dispersion clearly shows the Dirac surface states, reproduced from previous report [34]. TSS is short for topological surface states, DP is short for Dirac point. The dotted red line qualitatively marks the Fermi level from the ARPES measurements. (f) Photon energy dependent measurements apparently confirm the surface states nature of the α bands. The photon energy used ranges from 40 to 110 eV.

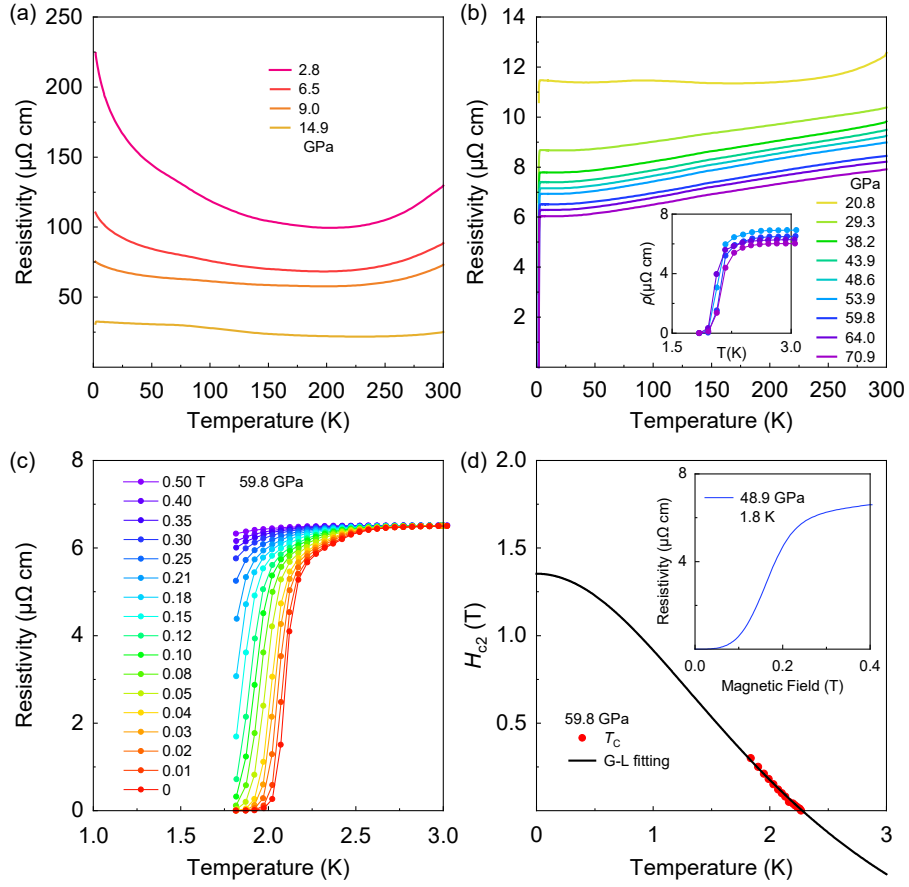


FIG. 3. Transport properties of SrIn₂As₂ as a function of pressure. (a) Electrical resistivity of SrIn₂As₂ as a function of temperature from 2.9 GPa to 14.9 GPa in run III. (b) Electrical resistivity of SrIn₂As₂ as a function of temperature from 20.8 GPa to 70.9 GPa in run III. Inset: Temperature-dependent resistivity of SrIn₂As₂ in the vicinity of the superconducting transition. (c) Resistivity as a function of temperature at the pressure of 59.8 GPa under different magnetic fields for SrIn₂As₂ in run III. (d) Temperature dependence of upper critical field for SrIn₂As₂ at 59.8 GPa. T_c is determined as the 90% drop of the normal state resistivity. The solid lines represent the Ginzburg-Landau (G-L) fitting. The $\mu_0 H_{c2}(0)$ is 1.35 T. Inset: Resistivity as a function of magnetic field at 1.8 K. The superconductivity state is suppressed for field sufficiently away from 0.4 T.

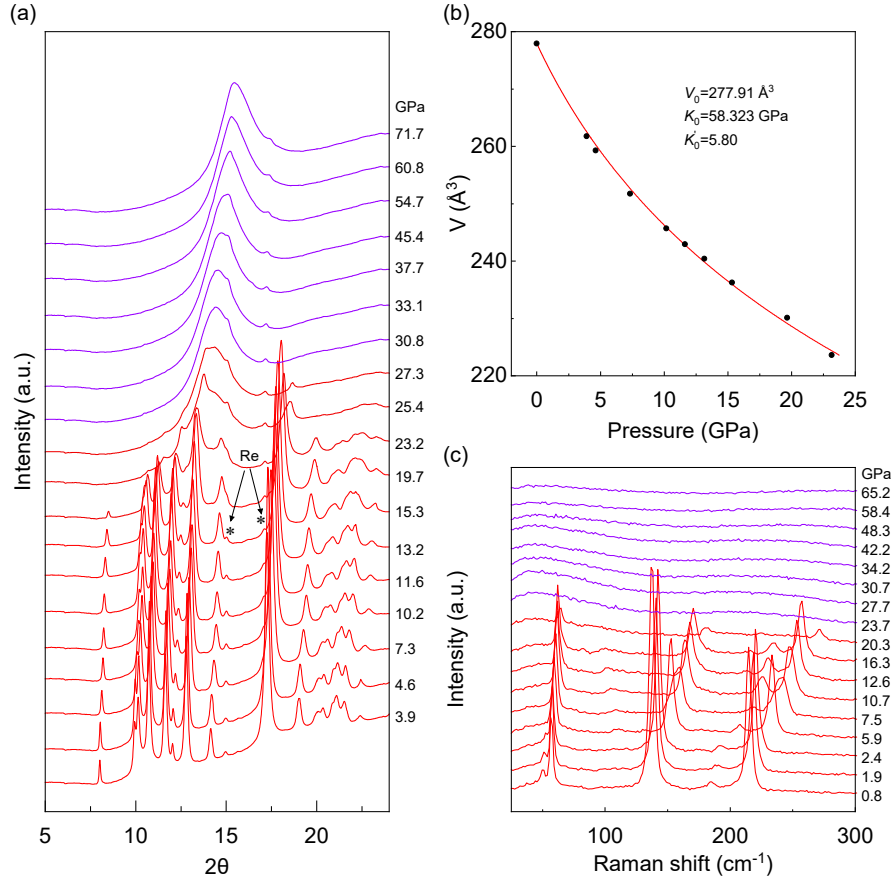


FIG. 4. (a) XRD patterns of SrIn₂As₂ under different pressures up to 71.7 GPa. (b) Variation in unit cell volume of SrIn₂As₂ with pressure at 300 K. Black circles: experiments. Solid lines are third-order Birch-Murnaghan fits to the data. The third-order Birch-Murnaghan equation of state (EOS) is given by $P = \frac{3}{2}K_0 \left[\left(\frac{V_0}{V}\right)^{\frac{7}{3}} - \left(\frac{V_0}{V}\right)^{\frac{5}{3}} \right] \left\{ 1 + \frac{3}{4}(K_0' - 4) \left[\left(\frac{V_0}{V}\right)^{\frac{2}{3}} - 1 \right] \right\}$. (c) Raman spectra of SrIn₂As₂ under pressure at room temperature.

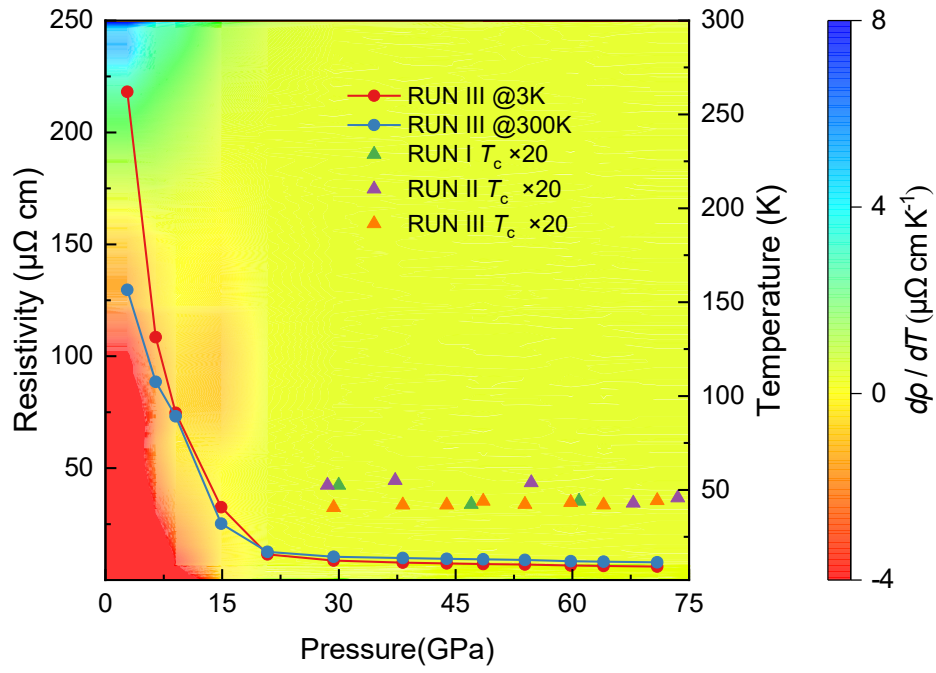


FIG. 5. Phase diagram of SrIn₂As₂. The red and blue dotted line plots represent the dependence of resistivity on temperature at 3 K and 300 K, respectively. Green, purple and orange triangle represent superconducting T_c in different runs, respectively. The background represents the dependence of $d\rho/dT$ on temperature at different pressures